frontiers in Chemistry

ORIGINAL RESEARCH
published: 12 September 2018
doi: 10.3389/fchem.2018.00351

The Activity Improvement of the TM_3(hexaiminotriphenylene)$_2$ Monolayer for Oxygen Reduction Electrocatalysis: A Density Functional Theory Study

Beibei Xiao[1], Hui Zhu[1], HouYi Liu[1], XiaoBao Jiang[2] and Qing Jiang[3]**

[1] School of Energy and Power Engineering, Jiangsu University of Science and Technology, Zhenjiang, China, [2] School of Materials Science and Engineering, Jiangsu University of Science and Technology, Zhenjiang, China, [3] Key Laboratory of Automobile Materials, Ministry of Education, School of Materials Science and Engineering, Jilin University, Changchun, China

OPEN ACCESS

Edited by:
Zhimin Ao, Guangdong University of Technology, China

Reviewed by:
Aijun Du, Queensland University of Technology, Australia
Simonetta Antonaroli, Università degli Studi di Roma Tor Vergata, Italy

***Correspondence:**
Beibei Xiao
xiaobb11@mails.jlu.edu.cn
Qing Jiang
jiangq@jlu.edu.cn

Specialty section:
This article was submitted to Green and Sustainable Chemistry, a section of the journal Frontiers in Chemistry

Received: *19 May 2018*
Accepted: *25 July 2018*
Published: *12 September 2018*

Citation:
Xiao B, Zhu H, Liu H, Jiang X and Jiang Q (2018) The Activity Improvement of the TM_3(hexaiminotriphenylene)$_2$ Monolayer for Oxygen Reduction Electrocatalysis: A Density Functional Theory Study. Front. Chem. 6:351. doi: 10.3389/fchem.2018.00351

Polymer electrolyte membrane fuel cells (PEMFCs) are one of the most prominent clean energy technologies designed to achieve hydrogen utilization and solve problems such as low efficiency and high pollution associated with fossil fuel combustion. In order to bring about PEMFC commercialization, especially for automobile applications, developing high-activity and -selectivity catalysts for the oxygen reduction reaction (ORR) is of critical importance. Based on the density functional theory, the catalytic activity of the conductive, two-dimensional metal–organic frameworks $TM_3(HITP)_2$ monolayer (where HITP = hexaiminotriphenylene; TM = Ni, Co, Fe, Pd, Rh, Ru, Pt, Ir, and Os) for ORR has been investigated systematically. Furthermore, the classical volcano curves of the ORR activity, as a function of the OH binding, are found where the Ni, Pd, and Pt located at the weak binding side suffer from the sluggish *OOH formation and prefer the inefficient $2e^-$ mechanism, while for other elements belonging to the strong binding side, the reactions are hindered by the poison due to ORR intermediates. Based on the free energy profiles, the corresponding overpotentials μ_{ORR} exhibit the inverted volcano curve as a function of the atomic number of the 3*d*/4*d*/5*d* TM active center in the same period. Based on the μ_{ORR} data, ORR activity decreases in the order of Ir > Co ≈ Rh > Ni ≈ Pd > Pt ≈ Fe > Ru > Os. Herein, the Co, Rh, and Ir central atoms exhibit enhanced catalytic activity in combination with the desirable selectivity of the O_2 reduction to H_2O. This systematic work may open new avenues for the development of high-performance non-PGM catalysts for practical applications of ORR.

Keywords: oxygen reduction reaction, activity and selectivity, 2D materials, transition metal elements, DFT calculation

INTRODUCTION

Hydrogen is a potential candidate for future energy provision, as stated in the concept of the hydrogen economy, so as to solve the issues of the rising global energy demands, depletion of fossil fuel reserves, and associated environmental pollution issues. Due to its high efficiency, ease of operation, and low emission, the polymer electrolyte membrane fuel cell (PEMFCs) is the

most prominent technology to derive benefit from the proposed hydrogen cycle, which leads to the production of electricity from the electrochemical oxidation of hydrogen, with water as its endproduct (Colić and Bandarenka, 2016; Xia Z. et al., 2016; Chen et al., 2017, 2018). However, a critical obstacle to its commercialization is the dominant voltage loss associated with the sluggish oxygen reduction reaction (ORR), even when catalyzed by the noble Pt nanoparticle (Nørskov et al., 2004). In this regard, a significant amount of Pt is required to achieve the desirable power density, making the overall cost prohibitively high (Debe, 2012). In order to overcome the economic bottleneck, design, and application of earth-abundant alternatives for ORR electrocatalysis are at the heart of PEMFC research (Xia W. et al., 2016).

Inspired by the pioneering work on cobalt phthalocyanines acting as cathode catalysts (Jasinski, 1964), a tremendous amount of research is being performed on the TM–N_x carbon materials for ORR (TM denotes transition metals), especially TM–N_4 active motif. The intrinsic active characteristic of TM in N_x carbon materials is experimentally supported, where the presence of the TM atom would boost the ORR performance compared with the metal-free counterpart (Peng et al., 2013; Yin et al., 2016; Yang et al., 2017); the corresponding activity would be suppressed by adding the SCN^- ions and CO molecule (Zhang et al., 2016; Yang et al., 2017). Linear correlations between the content of TM–N_x and ORR activity have been observed (Yang et al., 2017). Furthermore, ORR activity shows its dependence on the TM center atom, and this is supported by the density functional theory (DFT), a theoretical work of Rossmeisl et al., where the ORR activity of the TM–N_4 embedded graphene has been systematically investigated, and where the Fe, Ir, Mn, Ru, and Rh doping is identified as boosting the ORR (Calle-Vallejo et al., 2011). Additionally, the ORR mechanism is sensitive to the TM–N_4 active motif. Liu et al. have synthesized the Fe–N_x and Co–N_x doped carbon nanofiber and realized that the Fe–N_4 promotes $4e^-$ ORR in comparison with the $2e^-$ pathway of the Co–N_4 one (Liu et al., 2016). The same conclusion has been achieved by Kattel et al., where the O–O bond scission is presented and the efficient $4e^-$ reduction of O_2 to $2H_2O$ is preferred on the Fe–N_4 sites, but the reduction of O_2 to H_2O_2 is found enhanced on the Co–N_4 motif (Kattel et al., 2013, 2014).

Despite these encouraging research works, such TM–N_4 carbon materials generally suffer from low activity caused by the relatively few catalytic sites as well as the experimental challenge of the well-controlled active motif (Liang et al., 2013; Peng et al., 2013; Palaniselvam et al., 2016), reducing the competition with the state-of-the-art Pt/C catalysts. Paying attention to the high TM–N_4 density in combination with the electronic conductivity, Miner et al. have developed the attractive $Ni_3(HITP)_2$ as ORR electrocatalyst (Miner et al., 2016). However, the performance is far from satisfying expectations, with its incomplete oxidation of O_2 and the predominant production of H_2O_2 under the working potential (Miner et al., 2016). In this regard, utilizing the aforementioned information, the development of the efficient $TM_3(HITP)_2$ catalysts can be achieved via the variation of metal nodes (Choi et al., 2015; Zhang et al., 2015). It has naturally raised the interest to search for the optimal combinations of the $TM_3(HITP)_2$, possessing superior ORR activity as well as selectivity.

In the manuscript, DFT calculations are used within an electrochemical framework to analyze the ORR electrocatalysis over the $TM_3(HITP)_2$monolayer. In particular, the stability of the ORR intermediates is calculated, which allows to evaluate the thermodynamic ORR free energy and its overpotentials. The data provide the fundamental understanding of the mechanism of $Ni_3(HITP)_2$ and further identify optimal candidates as catalysts. According the *d*–partial density of states, an atomistic insight of the activity origin has been provided by a thorough comparison among the considered systems. Herein, for simplification, our attention is mainly focused on the monolayer structure shown in **Figure 1** as a representative model due to the weak interaction between the interlayers of the 2D-layered materials (Sheberla et al., 2014; Chen et al., 2015; Miner et al., 2016).

METHODS

All calculations have been performed within the DFT framework, as implemented in the DMol^3 code (Delley, 1990, 2000). The generalized gradient approximation with the Perdew–Burke–Ernzerhof (PBE) functional is employed to describe exchange and correlation effects (Perdew et al., 1996). The DFT semicore pseudopotentials (DSPP) core treat method is implemented for relativistic effects, which replaces core electrons by a single effective potential and introduces some degree of relativistic correction into the core (Delley, 2002). The double numerical atomic orbital augmented by a polarization function (DNP) is chosen as the basis set (Delley, 1990). A smearing of 0.005 Ha (1 Ha = 27.21 eV) to the orbital occupation is applied to achieve accurate electronic convergence. In order to ensure high-quality results, the real-space global orbital cutoff radius is set as high as 5.2 Å. In order to accurately describe the long-range electrostatic interactions of the ORR intermediates with catalysts, the PBE-D method with the TS van der Waals (vdW) correction is employed. In the geometry optimization of structures, the convergence tolerances of energy, maximum force, and displacement are

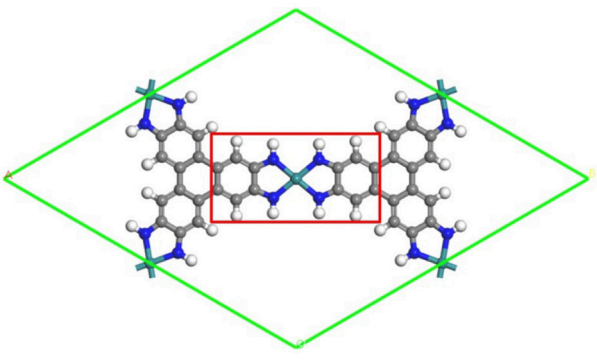

FIGURE 1 | The schematic structure of the $TM_3(HITP)_2$ monolayer. Green, blue, gray, and white denote the TM, N, C, and H atoms.

1.0×10^{-5} Ha, 0.002 Ha/Å, and 0.005 Å, respectively. The spin-unrestricted method is used for all calculations. A conductor-like screening model (COSMO) was used to simulate a H_2O solvent environment for all calculations (Todorova and Delley, 2008), which is a continuum model, where the solute molecule forms a cavity within the dielectric continuum. The DMol^3/COSMO method has been generalized to periodic boundary cases. The dielectric constant is set as 78.54 for H_2O. Some previous results have shown that this implicit solvation model is an effective method to describe solvation (Sha et al., 2011; Zhang et al., 2015). The 15 Å-thick vacuum is added to avoid the artificial interactions between the $TM_3(HITP)_2$ monolayer and its images. The proposed structure of the $TM_3(HITP)_2$ monolayer is shown in **Figure 1**, where the atoms in the red square are fixed in all of the structure-optimization calculations.

The adsorption energy (E_{ads}) of the reactant O_2 is calculated by the following,

$$E_{ads}(O_2) = E_{sys} - E_{substrate} - E_{O2} \quad (1)$$

The adsorption energy (E_{ads}) of the ORR intermediates are calculated relative to H_2O and H_2 (Calle-Vallejo et al., 2011), through,

$$E_{ads}(OOH) = E_{sys} - E_{substrate} - (2E_{H2O} - 3/2E_{H2}) \quad (2)$$

$$E_{ads}(O) = E_{sys} - E_{substrate} - (E_{H2O} - E_{H2}) \quad (3)$$

$$E_{ads}(OH) = E_{sys} - E_{substrate} - (E_{H2O} - 1/2E_{H2}) \quad (4)$$

where E_{sys}, $E_{substrate}$, E_{H2O}, and E_{H2} are the total energy of the adsorption systems, the $TM_3(HITP)_2$ monolayer, H_2O molecule, and H_2 molecule, respectively. The $E_{ads} < 0$ corresponds to an exothermic adsorption process.

The Gibbs free energy changes (ΔG) of the ORR elemental steps have been calculated according to the computational hydrogen electrode (CHE) model developed by Nørskov et al., where the chemical potential of the proton/electron ($H^+ + e^-$) in solution is equal to the half of the chemical potential of a gas-phase H_2 at the reference relative hydrogen electrode (RHE) potential (Nørskov et al., 2004). Herein, $G_{(H++e-)} = 1/2G_{(H2)}$. The variance of the proton–electron pair free energy with potential is simply determined using the linear free energy dependence of the electron energy on potential, shifting the electron energy $-eU$, where e is the elementary positive charge and U is the electrode potential of interest on the RHE scale (Nørskov et al., 2004; Nie et al., 2014). The total chemical potential of a proton–electron pair at the potential U is written as follows:

$$G(U)_{(H++e-)} = 1/2G_{(H2)} - eU \quad (5)$$

Therefore, for a general electrochemical reaction, the free energy change ΔG for every elemental step can be determined as following:

$$\Delta G = \Delta E + \Delta ZPE - T\Delta S + \Delta G_{pH} + \Delta G_U \quad (6)$$

where ΔE is the electronic energy difference based on DFT calculations, ΔZPE is the change in zero point energy, T is the temperature (equal to 298.15 K here), ΔS is the change in the entropy, and ΔG_{pH} and ΔG_U are the free energy contributions due to variation in pH value and electrode potential U, respectively. $\Delta G_U = -eU$, in which U is the potential related to the standard hydrogen electrode. $\Delta G_{pH} = -kT\ln10$ x pH, which is the corrected free energy of H^+ ions depending on the concentration. According to the previous works, pH is set as 0 in acid medium and 14 in alkaline medium. The zero-point energies and entropies of the ORR intermediates are calculated from the vibrational frequencies according to standard methods. Following the suggestion of Wilcox et al. (Lim and Wilcox, 2012), in order to reduce the calculation, the $TM_3(HITP)_2$ monolayer is fully constrained. The $\Delta G < 0$ corresponds to an exothermic adsorption process. The free energy G of O_2 is derived as $G(O_2) = 4.92+2G(H_2O)-2G(H_2)$ by utilizing OER equilibrium at the standard conditions; the G of H_2O_2 is derived similarly considering that the H_2O_2/O_2 standard equilibrium potential is 0.682 V vs. SHE (Sun et al., 2014). The CHE model has been successfully applied for developing the novel electrocatalysts with prominent ORR performances, where the DFT calculations are in line with the experimental results (Nørskov et al., 2004; Greeley et al., 2009; Favaro et al., 2015; Lang et al., 2015; Jia et al., 2016; Tang et al., 2016; Liu et al., 2017; Li et al., 2018; Xu et al., 2018). Furthermore, the PBE/DNP method in Dmol^3 code has been widely employed for evaluating the potential of the TM-based carbon electrocatalysts (Wang et al., 2015, 2016b; Hou et al., 2016; Xiao et al., 2017). Therefore, the reliability of the mentioned approach is confirmed.

RESULTS AND DISCUSSION

Prior to the investigation of the activity, the essential step is to determine the adsorption behavior of the ORR intermediates. For $Ni_3(HITP)_2$, the energetics of the O_2 adsorption is endothermic with the value of 0.13 eV, caused by the structure deformation as shown in the inset of **Figure 2A**, indicating no such adsorption has occurred on the Ni center atom. Besides the reactant, the corresponding E_{ads} of ORR intermediates are 4.08, 3.57, and 1.17 eV for OOH, O, and OH, respectively. In comparison with the Pt(111) (3.55 eV for OOH, 1.38 eV for O, and 0.64 eV for OH) (Xiao et al., 2016), the obviously weak adsorption ability of the center Ni atom has been observed.

Considering the low affinity of the ORR intermediates to the Ni center, it is expected that the ORR activity would be boosted by selecting suitable TMs. Indeed, the change of the TM center definitely exhibits different adsorption behaviors, as shown in **Figure 2**, where the corresponding E_{ads} data are given. From the figures, the E_{ads} of the reactant O_2 and the corresponding ORR intermediates decrease monotonically in the order of Ru ≈ Os > Fe > Co > Rh ≈ Ir > Ni > Pd ≈ Pt. It is obvious that the adsorption ability of the elements is weakened from group 8 to group 10. Carefully reviewing the O_2 adsorption as shown in the inset of **Figure 2A**, similar to Ni, no such adsorption behaviors have occurred at the Pd and Pt active centers due to the endothermic adsorption energies. The unfavorable adsorption behavior of group 10 implies the

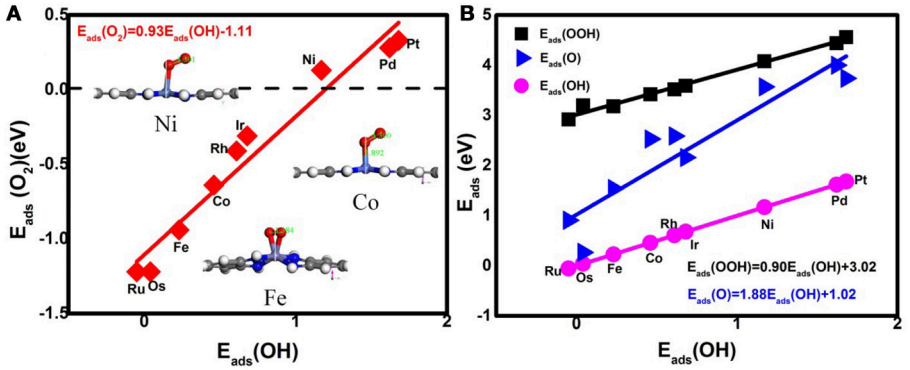

FIGURE 2 | The adsorption energies of the O_2 molecules **(A)** and the ORR intermediates **(B)**. Inset: the representative O_2 adsorption structure on Ni, Co, and Fe active centers.

underlying mechanism of the OOH formation, which originates from the long-range electron transfer from the catalyst to O_2 molecules at the outer Helmholtz plane (Choi et al., 2014). On the contrary, group 9 binds to the reactant suitably with the corresponding end-on structure and group 8 possesses a too strong O_2 adsorption with the side-on adsorption configuration. Herein, the mentioned adsorption capability is in line with the general prediction of the *d*-band model (Hammer and Nørskov, 2000). The corresponding evidences are provided by the *d*–partial density of states (*d*–PDOS) of the central TM atom plotted in **Figure 3**. As shown, the *d* band moves away from the Fermi energy as the TM atom changes from group 8 to group 10. The TM atom with the higher *d* states possesses stronger adsorption ability. Furthermore, due to the relationship between the adsorption behavior and the *d* band, the linear scaling relations between $E_{ads}(O_2)/E_{ads}(OOH)/E_{ads}(O)$ and $E_{ads}(OH)$ are observed, in accordance with the previous reports of other functionalized carbon materials (Calle-Vallejo et al., 2011; Baran et al., 2014). That is,

$$E_{ads}(O_2) = 0.93E_{ads}(OH) - 1.11, \quad (7)$$

$$E_{ads}(OOH) = 0.90E_{ads}(OH) + 3.02, \quad (8)$$

$$E_{ads}(O) = 1.88E_{ads}(OH) + 1.02. \quad (9)$$

To further evaluate the ORR activity of $TM_3(HITP)_2$, according to the experimental condition (Miner et al., 2016), the OOH associative mechanisms in the alkaline solution are taken into consideration, with the elemental steps R_i listed as follows (Wang et al., 2016a), where asterisks denote active TM sites. Due to the small barrier of proton transfer, which can be ignored at high applied voltages, our attention is only focused on the reaction energies (Nørskov et al., 2004; Calle-Vallejo et al., 2011; Zhang et al., 2015).

$$O_2(g) + * + H_2O(l) + e^- \rightarrow OOH^* + OH^-, (R_1)$$

$$OOH^* + e^- \rightarrow O^* + OH^-, \quad (R_{2a})$$

$$OOH^* + H_2O(l) + e^- \rightarrow H_2O_2^* + OH^-, \quad (R_{2b})$$

$$O^* + H_2O(l) + e^- \rightarrow OH^* + OH^-, \quad (R_3)$$

$$OH^* + e^- \rightarrow OH^-. \quad (R_4)$$

Analyzing the free energy plots of the complete $4e^-$ ORR pathway in **Figure 4A**, the endothermic processes of *OOH formation (R_1) and *O formation (R_{2a}) are observed even at $U = 0$ V. The corresponding values of the free energy change ΔG_i are 0.28 and 0.08 eV, respectively. The positive values indicate that the mentioned steps are thermodynamically unfavorable (Nørskov et al., 2004). When the ideal potential of 0.4 eV is applied, the mentioned reaction steps are even unfavorable with the increased ΔG_i of 0.68 and 0.48 eV, respectively. Based on the information, R_1 is determined as the rate-determining step (RDS), pointing to the fact that the $Ni_3(HITP)_2$ monolayer suffers from insufficient O_2 activation (Greeley et al., 2009), in accordance with the endothermic capture of the O_2 molecule as shown in **Figure 2A**. To clarify the selectivity of the $2/4e^-$ mechanism, the comparison between R_{2a} and R_{2b} is considered. In the alternative $2e^-$ pathway, the ΔG_{2b} of the H_2O_2 formation (R_{2b}) is increased from 0.01 to 0.41 eV as the *U* ranged from 0 to 0.4 V, being 0.07 eV lower than ΔG_{2a}, indicating the slightly energy favorable condition of R_{2b}. Herein, the predominant production of H_2O_2 would be expected on the $Ni_3(HITP)_2$ monolayer, which is in consistence with the experiment results of the 3D $Ni_3(HITP)_2$. In summary, the $Ni_3(HITP)_2$ monolayer slightly prefers the $2e^-$ mechanism, with the RDS located at the *OOH formation.

Owing to the different adsorption abilities of $TM_3(HITP)_2$, the suitable TM would boost the ORR activity as well as the selectivity of the $4e^-$ mechanism. In order to characterize the relationship between the ORR activity and the TM center atom, the reactive free energy change ΔG_i of the elementary steps R_i at $U = 0.4$ V as a function of $E_{ads}(OH)$ is plotted in **Figure 4B**. As the weakening of the $E_{ads}(OH)$ occurs with the values ranging from −0.05 to 1.68 eV, ΔG_1 and ΔG_{2a} increase from the negative to the positive values, while the opposite tendency is found for ΔG_3 and ΔG_4, which decrease from the positive to the negative values. That is, the steps R_1 and R_{2a} change from the exothermic to endothermic process, while the steps R_3 and R_4 become more thermodynamically favorable. Obviously, the RDS steps are identified as R_4 for group 8 and group 9 with the exception of Os, where the RDS step is R_3, while the RDS step is located at R_1 for group 10.

On the basis of the assumption that the activation barrier for the RDS is equal to ΔG_{max}, the activity variation of $TM_3(HITP)_2$ referred to as $Ni_3(HITP)_2$ is estimated by the rate constant k via the simple Arrhenius equation in the following,

$$k = A\exp(-\Delta G_{max}/k_BT) \quad (10)$$

$$\ln(k_{TM}/k_{Ni}) = [\Delta G_{max}(Ni) - \Delta G_{max}(TM)]/k_BT \quad (11)$$

where A is the prefactor, k_B is the Boltzmann constant, and T is the temperature (298.15 K). The classic volcano curve is observed in **Figure 5A**, where the $\ln(k_{TM}/k_{Ni})$ as a function of the E_{ads}(OH) is plotted. Based on our results, the adsorption ability is weakened as the atomic number increases from group 8 to group 10. The Ni/Pd/Pt active centers suffer from the too weak binding strength, leading to the energetically unfavorable process of the *OOH formation. Meanwhile, for the Fe/Ru/Os active centers, the too strong interaction with the ORR intermediates accounts for the poisoning of the O-containing intermediates. The suitable binding strength of Co/Rh/Ir active centers indicates the balance between the O_2 activation and the catalyst recovery.

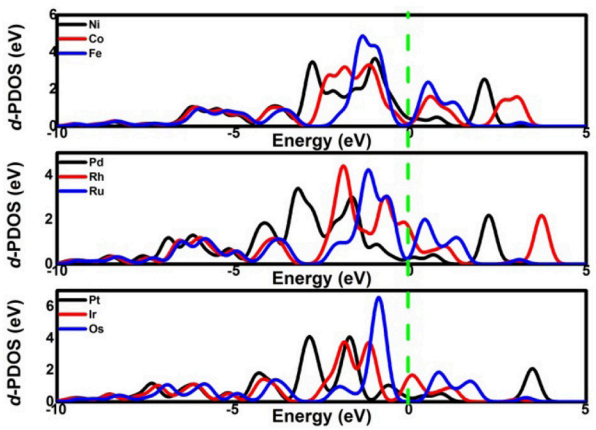

FIGURE 3 | The *d*-PDOS of the central TM atom.

As discussed by the previous reports (Calle-Vallejo et al., 2011; Viswanathan et al., 2012a; Baran et al., 2014; Zhang et al., 2015), the ORR activity depends on the adsorption of the intermediates. Our results are in accordance with the previous reports in that the bond strength should be compromised in the case of the effective ORR catalysts on the basis of Sabatier principle (Greeley et al., 2009; Gao et al., 2017, 2018); this is similar with the previous studies on metal (Stephens et al., 2012), functional graphene (Calle-Vallejo et al., 2011), metal porphyrine (Baran et al., 2014) as well as the 2D MOF (Gao et al., 2017). Herein, in comparison with the $Ni_3(HITP)_2$ monolayer (0.68 eV), group 9 possesses superior catalytic performance with the smaller ΔG_{max} of 0.50, 0.52, and 0.22 eV for the Co, Rh, and Ir center atoms, respectively. By contrast, inferior activities are observed for group 8 and group 10. The corresponding ΔG_{max} are 0.93, 1.23, and 1.34 eV for Fe, Ru, and Os atoms, and 0.72 and 0.90 eV for Pd and Pt atoms, respectively. Furthermore, for clarification, the data of the relative overpotentials μ_{ORR} are summarized and collected for the activity comparison, depicted in **Figure 6**. As the atomic number of TM increased from Ni to Fe, the μ_{ORR} reduces and then increases, presenting further evidence to the presence of the classical volcano-shaped activity (Nørskov et al., 2004; Calle-Vallejo et al., 2011; Baran et al., 2014; Zheng et al., 2017). Similar situations are found for the 4*d*/5*d* $TM_3(HITP)_2$ monolayer. Based on the μ_{ORR} data, ORR activity decreases in the order of Ir > Co ≈ Rh > Ni ≈ Pd > Pt ≈ Fe > Ru > Os. Furthermore, compared with the data of the TM supported on graphene and macrocyclic molecules (the minimum μ_{ORR} = 0.4 eV) (Xu et al., 2018), the prominent improvement of the ORR activity on the $Ir_3(HITP)_2$ monolayer is confirmed.

Besides the ORR activity, the ORR selectivity is characterized by the ratio of the corresponding reaction rate k_{2a} (k_{2b}) for step R_{2a} (R_{2b}), via the following equation,

$$\ln(k_{2a}/k_{2b}) = [\Delta G_{2b} - \Delta G_{2a}]/k_BT \quad (12)$$

The data are plotted in **Figure 5B**. As shown, $\ln(k_{2a}/k_{2b})$ shows a linear relationship with E_{ads}(OH). For the weak side, the values of ΔG_{2a} and ΔG_{2b} are 0.48 and 0.41 eV for Ni, 0.57 and 0.37 eV for Pd, and 0.20 and 0.19 eV for Pt, respectively. The corresponding

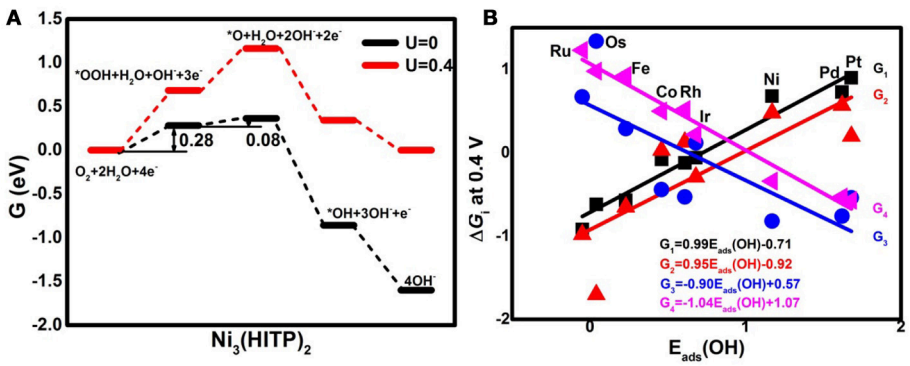

FIGURE 4 | The free energy *G* diagrams of $Ni_3(HITP)_2$ in the alkaline medium **(A)** and the free energy change ΔG_i of the elemental step R_i at the ideal potential of 0.4 eV **(B)**.

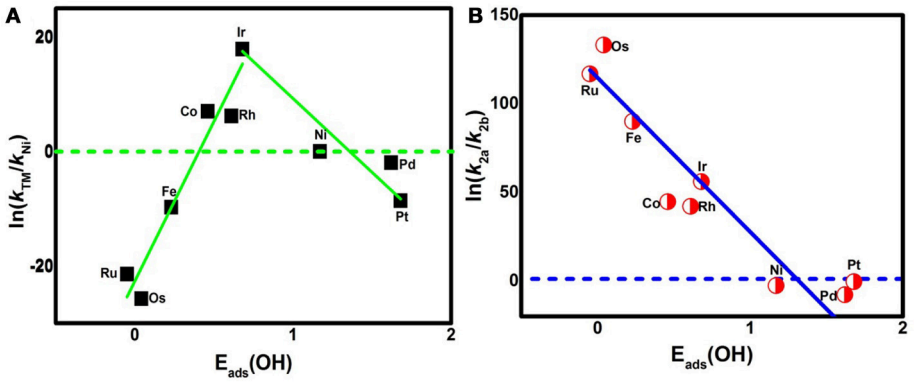

FIGURE 5 | The activity enhancement factor of $TM_3(HITP)_2$ referred to the $Ni_3(HITP)_2$ **(A)** and the selectivity of the $4e^-$ reduction referred to the $2e^-$ pathway **(B)**.

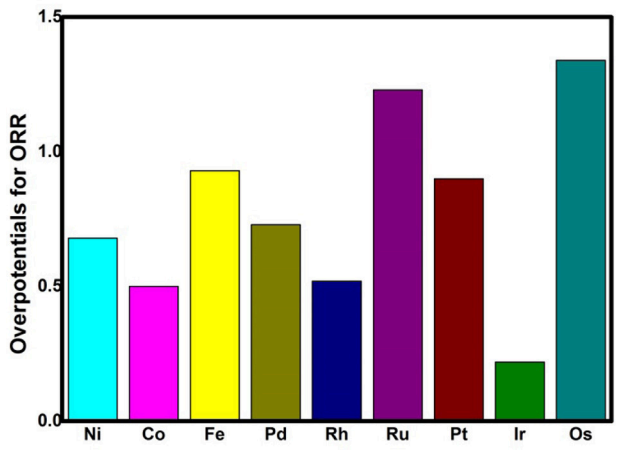

FIGURE 6 | The overpotentials μ_{ORR} of the $TM_3(HITP)_2$ monolayer for the $4e^-$ mechanism.

TABLE 1 | The E_{ads} and ΔG of ORR intermediates at the potential $U = 0.4$V with and without the vdW corrections.

	Without vdW			With vdW		
	Co	Rh	Ir	Co	Rh	Ir
E_{ads} (O_2)	−0.64	−0.41	−0.31	−0.67	−0.50	−0.39
E_{ads} (OOH)	3.42	3.52	3.59	3.20	3.41	3.49
E_{ads} (O)	2.53	2.59	2.16	2.54	2.55	2.11
E_{ads} (OH)	0.46	0.61	0.68	0.28	0.54	0.61
ΔG_1	−0.08	−0.12	−0.06	−0.31	−0.23	−0.16
ΔG_{2a}	0.03	0.13	−0.29	0.26	0.20	−0.23
ΔG_{2b}	1.18	1.21	1.15	1.40	1.32	1.26
ΔG_3	−0.44	−0.53	0.12	−0.64	−0.56	0.09
ΔG_4	0.50	0.52	0.22	0.68	0.59	0.30
ΔG_{max}	0.50	0.52	0.22	0.68	0.59	0.30

$\ln(k_{2a}/k_{2b})$ are −2.72, −7.78, and −0.39, indicating the energy favorability of R_{2b} compared with that of R_{2a} for group 10. Furthermore, considering the $\ln(k_{2a}/k_{2b})$ data, the $2e^-$ reduction of O_2 to H_2O_2 is prevalent at the Ni and Pd centers, while the mixing of $2/4e^-$ ORR is reasonable for the Pt center. By contrast, R_{2a} is preferred for other elements indicated by the positive $\ln(k_{2a}/k_{2b})$. That is, the $4e^-$ mechanism is dominant for group 8 and group 9. Obviously, as the E_{ads}(OH) is strengthened, the catalytic selectivity is changed from the $2e^-$ to $4e^-$ pathway. The two sides of the catalytic activity profile shown in **Figure 5A** essentially distinguish the $2e^-$ catalysts (weak binding side) from the $4e^-$ catalysts (strong binding side) (Viswanathan et al., 2012b; Zagal and Koper, 2016). That is, the former suffering from the insufficient O_2 activation favors the H_2O_2 formation; the latter poisoned by the O–containing intermediates generally prefers the H_2O formation. The formation of H_2O_2 not only decreases the ORR efficiency, but also degrades the proton exchange membrane (Tsuneda et al., 2017). In short, the dramatic enhancements in oxygen-reduction rates and product selectivity are achieved by selecting TM centers in group 9, in line with the previous works (Gao et al., 2017; Wannakao et al., 2017).

To understand the influence of the long-term electrostatic potential on the ORR performance, the vdW correction is further applied for analyzing the optimum Ir/Co/Rh systems, where the corresponding adsorption energy and the free energy changes are listed in **Table 1**. Intuitively, the adsorption abilities of the mentioned systems are enhanced due to the presence of the long-term interaction, in consistence with our calculation data. For the $Ir_3(HITP)_2$ monolayer, the E_{ads} are slightly increased to −0.39, 3.49, 2.11, and 0.61 eV for O_2, OOH, O, and OH, respectively, in comparison with the uncorrected values of −0.31, 3.59, 2.16, and 0.68 eV. The perturbation of the binding strength hinders the OH removal from the Ir active site, leading to the uphill of the ΔG_{max} from 0.22 to 0.30 eV. Despite the activity decrease, the $4e^-$ reduction pathway remains, supported by the values of ΔG_{2a} with −0.23 eV and ΔG_{2b} with 1.26 eV. Herein, the same phenomenon is found for $Co_3(HITP)_2$ and $Rh_3(HITP)_2$ with the ΔG_{max} of 0.68 and 0.59 eV, respectively. The corresponding ORR activity with th $4e^-$ reaction mechanism follows the order of Ir > Rh ≈ Co. Despite the numerical variation, the trend

is roughly consistent with the results without considering vdW interaction.

Despite the presence of the $Ni_3(HITP)_2$ experimentally, other 2D catalysts are only theoretical models, which need the confirmation of their synthesis. It should be noted that changing metal atoms would significantly modify the corresponding structures. Thus, by replacing the Ni central atom, the dimensionality of the $Cr_3(HITP)_2$ could be transferred from 2D to 3D due to the energetic favorable insertion of the spacer linker (Foster et al., 2016). Different structures inevitably lead to distinct catalytic performances (Sun et al., 2014). In this regard, although the theoretical candidates have been rationally predicted, the ORR performance of the optimum $TM_3(HITP)_2$ with the Co/Rh/Ir active sites crucially needs further experimentally verification.

CONCLUSION

Based on the DFT, the ORR mechanisms on $TM_3(HITP)_2$ monolayer have been studied. It is found that the selection of central metals affects the adsorption behaviors, tuning ORR activity and its selectivity. It is realized that the adsorption abilities are monotonously enhanced as the *d* band upshifts from group 10 to group 8. A classical volcano relationship for the predicted ORR activity as a function of calculated OH adsorption energy is observed. From the calculated ΔG data, the ORR activity decreases in the order of Ir > Co ≈ Rh > Ni ≈ Pd > Pt ≈ Fe > Ru > Os. That is, group 9 possesses superior activity compared with other elements. Furthermore, owing to the insufficient O_2 activation, the $2e^-$ mechanism is prevalent in group 10, while the desirable $4e^-$ mechanism is dominant for others. These results would throw insights into the nature of the ORR mechanisms of $TM_3(HITP)_2$. The materials of the $Co_3(HITP)_2$, $Rh_3(HITP)_2$, and $Ir_3(HITP)_2$ have been screened out and served as the potential candidates for the ORR electrocatalysis.

AUTHOR CONTRIBUTIONS

BX carried out the simulation and wrote the paper. QJ revised the paper. HZ, HL, and XJ entered the discussion. All authors commented on the manuscript.

ACKNOWLEDGMENTS

We acknowledge the support from the National Natural Science Foundation of China (No. 21503097, 51631004) and the Natural Science Foundation of Jiangsu (No.BK20140518).

REFERENCES

Baran, J. D., Grönbeck, H., and Hellman, A. (2014). Analysis of porphyrines as catalysts for electrochemical reduction of O_2 and oxidation of H_2O. *J. Am. Chem. Soc.* 136, 1320–1326. doi: 10.1021/ja4060299

Calle-Vallejo, F., Martinez, J. I., and Rossmeisl, J. (2011). Density functional studies of functionalized graphitic materials with later transition metals for oxygen reduction reaction. *Phys. Chem. Chem. Phys.* 13, 15639–15643. doi: 10.1039/c1cp21228a

Chen, D., Xu, Y., Hu, B., Yan, C., and Lu, L. (2018). Investigation of proper external air flow path for tubular fuel cell stacks with an anode support feature. *Energ. Convers. Manage.* 171, 807–814. doi: 10.1016/j.enconman.2018.06.036

Chen, D., Xu, Y., Tade, M. O., and Shao, Z. (2017). General regulation of air flow distribution characteristics within planar solid oxide fuel cell stacks. *ACS Energy Lett.* 2, 319–326. doi: 10.1021/acsenergylett.6b00548

Chen, S., Dai, J., and Zeng, X. C. (2015). Metal–organic kagome lattices M_3(2,3,6,7,10, 11-hexaiminotriphenylene)$_2$ (M= Ni and Cu): from semiconducting to metallic by metal substitution. *Phys. Chem. Chem. Phys.* 17, 5954–5958. doi: 10.1039/C4CP05328A

Choi, C. H., Lim, H. K., Chung, M. W., Park, J. C., Shin, H., Kim, H., et al. (2014). Long-range electron transfer over graphene-based catalyst for high-performing oxygen reduction reactions: importance of size, N-doping, and metallic impurities. *J. Am. Chem. Soc.* 136, 9070–9077. doi: 10.1021/ja5033474

Choi, W. I., Wood, B. C., Schwegler, E., and Ogitsu, T. (2015). Combinatorial search for high-activity hydrogen catalysts based on transition-metal-embedded graphitic carbons. *Adv. Energy. Mater.* 5:1501423. doi: 10.1002/aenm.201501423

Colić, V., and Bandarenka, A. S. (2016). Pt alloy electrocatalysts for oxygen reduction reaction: from model surfaces to nanostructured systems. *ACS Catal.* 6, 5378–5385. doi: 10.1021/acscatal.6b00997

Debe, M. K. (2012). Electrocatalyst approaches and challenges for automotive fuel cells. *Nature* 486, 43–51. doi: 10.1038/nature11115

Delley, B. (1990). An all-electron numerical method for solving the local density functional for polyatomic molecules. *J. Chem. Phys.* 92, 508–517. doi: 10.1063/1.458452

Delley, B. (2000). From molecules to solids with the $DMol^3$ approach. *J. Chem. Phys.* 113, 7756–7764. doi: 10.1063/1.1316015

Delley, B. (2002). Hardness conserving semilocal pseudopotentials. *Phys. Rev. B* 66:155125. doi: 10.1103/PhysRevB.66.155125

Favaro, M., Ferrighi, L., Fazio, G., Colazzo, L., Di Valentin, C., Durante, C., et al. (2015). Single and multiple doping in graphene quantum dots: unraveling the origin of selectivity in the oxygen reduction reaction. *ACS Catal.* 5, 129–144. doi: 10.1021/cs501211h

Foster, M. E., Sohlberg, K., Spataru, C. D., and Allendorf, M. D. (2016). Proposed modification of the graphene analogue $Ni_3(HITP)_2$ to yield a semiconducting material. *J. Phys. Chem. C* 120, 15001–15008. doi: 10.1021/acs.jpcc.6b05746

Gao, G., Bottle, S., and Du, A. (2018). Understanding the activity and selectivity of single atom catalysts for hydrogen and oxygen evolution via ab initial study. *Catal. Sci. Technol.* 8, 996–1001. doi: 10.1039/C7CY02463K

Gao, G., Waclawik, E. R., and Du, A. (2017). Computational screening of two-dimensional coordination polymers as efficient catalysts for oxygen evolution and reduction reaction. *J. Catal.* 352, 579–585. doi: 10.1016/j.jcat.2017.06.032

Greeley, J., Stephens, I. E. L., Bondarenko, A. S., Johansson, T. P., Hansen, H. A., Jaramillo, T. F., et al. (2009). Alloys of platinum and early transition metals as oxygen reduction electrocatalysts. *Nat. Chem.* 1, 552–556. doi: 10.1038/nchem.367

Hammer, B., and Nørskov, J. K. (2000). Theoretical surface science and catalysis-calculations and concepts. *Adv. Catal.* 45, 71–129. doi: 10.1016/S0360-0564(02)45013-4

Hou, X., Zhang, P., Li, S., and Liu, W. (2016). Enhanced electrocatalytic activity of nitrogen-doped olympicene/graphene hybrids for the oxygen reduction reaction. *Phys. Chem. Chem. Phys.* 18, 22799–22804. doi: 10.1039/C6CP03451A

Jasinski, R. (1964). A new fuel cell cathode catalyst. *Nature* 201, 1212–1213. doi: 10.1038/2011212a0

Jia, Y., Zhang, L., Du, A., Gao, G., Chen, J., Yan, X., et al. (2016). Defect graphene as a trifunctional catalyst for electrochemical reactions. *Adv. Mater.* 28, 9532–9538. doi: 10.1002/adma.201602912

Kattel, S., Atanassov, P., and Kiefer, B. (2013). Catalytic activity of Co-Nx/C electrocatalysts for oxygen reduction reaction: a density functional theory study. *Phys. Chem. Chem. Phys.* 15, 148–153. doi: 10.1039/C2CP42609A

Kattel, S., Atanassov, P., and Kiefer, B. (2014). A density functional theory study of oxygen reduction reaction on non-PGM Fe-Nx-C electrocatalysts. *Phys. Chem. Chem. Phys.* 16, 13800–13806. doi: 10.1039/c4cp01634c

Lang, X. Y., Han, G. F., Xiao, B. B., Gu, L., Yang, Z. Z., Wen, Z., et al. (2015). Mesostructured intermetallic compounds of platinum and non-transition metals for enhanced electrocatalysis of oxygen reduction reaction. *Adv. Funct. Mater.* 25, 230–237. doi: 10.1002/adfm.201401868

Li, F., Han, G. F., Noh, H. J., Kim, S.-J., Lu, Y., Jeong, H. Y., et al. (2018). Boosting oxygen reduction catalysis with abundant copper single atom active sites. *Energy Environ. Sci.* 11, 2263–2269. doi: 10.1039/C8EE01169A

Liang, H. W., Wei, W., Wu, Z.-S., Feng, X., and Müllen, K. J. (2013). Mesoporous metal-nitrogen-doped carbon electrocatalysts for highly efficient oxygen reduction reaction. *J. Am. Chem. Soc.* 135, 16002–16005. doi: 10.1021/ja407552k

Lim, D. H., and Wilcox, J. (2012). Mechanisms of the oxygen reduction reaction on defective graphene-supported Pt nanoparticles from first-principles. *J. Phys. Chem. C* 116, 3653–3660. doi: 10.1021/jp210796e

Liu, J., Jiao, M., Lu, L., Barkholtz, H. M., Li, Y., Wang, Y., et al. (2017). High performance platinum single atom electrocatalyst for oxygen reduction reaction. *Nat. Commun.* 8:15938. doi: 10.1038/ncomms15938

Liu, K., Kattel, S., Mao, V., and Wang, G. (2016). Electrochemical and computational study of oxygen reduction reaction on nonprecious transition metal/nitrogen doped carbon nanofibers in acid medium. *J. Phys. Chem. C* 120, 1586–1596. doi: 10.1021/acs.jpcc.5b10334

Miner, E. M., Fukushima, T., Sheberla, D., Sun, L., Surendranath, Y., and Dincă, M. (2016). Electrochemical oxygen reduction catalysed by Ni_3(hexaiminotriphenylene)$_2$. *Nat. Commun.* 7:10942. doi: 10.1038/ncomms10942

Nie, X., Luo, W., Janik, M. J., and Asthagiri, A. (2014). Reaction mechanisms of CO_2 electrochemical reduction on Cu (1 1 1) determined with density functional theory. *J. Catal.* 312, 108–122. doi: 10.1016/j.jcat.2014.01.013

Nørskov, J. K., Rossmeisl, J., Logadottir, A., Lindqvist, L., Kitchin, J. R., Bligaard, T., et al. (2004). Origin of the overpotential for oxygen reduction at a fuel–cell cathode. *J. Phys. Chem. B* 108, 17886–17892. doi: 10.1021/jp047349j

Palaniselvam, T., Kashyap, V., Bhange, S. N., Baek, J. B., and Kurungot, S. (2016). Nanoporous graphene enriched with Fe/Co-N active sites as a promising oxygen reduction electrocatalyst for anion exchange membrane fuel cells. *Adv. Funct. Mater.* 26, 2150–2162. doi: 10.1002/adfm.201504765

Peng, H., Mo, Z., Liao, S., Liang, H., Yang, L., Luo, F., et al. (2013). High performance Fe- and N- doped carbon catalyst with graphene structure for oxygen reduction. *Sci. Rep.* 3:1765. doi: 10.1038/srep01765

Perdew, J. P., Burke, K., and Ernzerhof, M. (1996). Generalized gradient approximation made simple. *Phys. Rev. Lett.* 77, 3865–3868. doi: 10.1103/PhysRevLett.77.3865

Sha, Y., Yu, T. H., Merinov, B. V., Shirvanian, P., and Goddard, W. A. (2011). Oxygen hydration mechanism for the oxygen reduction reaction at Pt and Pd fuel cell catalysts. *J. Phys. Chem. Lett.* 2, 572–576. doi: 10.1021/jz101753e

Sheberla, D., Sun, L., Blood-Forsythe, M. A., Er, S., Wade, C. R., Brozek, C. K., et al. (2014). High electrical conductivity in Ni_3(2,3,6,7,10,11-hexaiminotriphenylene)$_2$, a semiconducting metal-organic graphene analogue. *J. Am. Chem. Soc.* 136, 8859–8862. doi: 10.1021/ja502765n

Stephens, I. E. L., Bondarenko, A. S., Grønbjerg, U., Rossmeisl, J., and Chorkendorff, I. (2012). Understanding the electrocatalysis of oxygen reduction on platinum and its alloys. *Energy Environ. Sci.* 5, 6744–6762. doi: 10.1039/C2EE03590A

Sun, J., Fang, Y., and Liu, Z. (2014). Electrocatalytic oxygen reduction kinetics on Fe-center of nitrogen-doped graphene. *Phys. Chem. Chem. Phys.* 16, 13733–13740. doi: 10.1039/C4CP00037D

Tang, C., Wang, H. F., Chen, X., Li, B. Q., Hou, T. Z., Zhang, B., et al. (2016). Topological defects in metal-free nanocarbon for oxygen electrocatalysis. *Adv. Mater.* 28, 6845–6851. doi: 10.1002/adma.201601406

Todorova, T., and Delley, B. (2008). Wetting of paracetamol surfaces studied by DMol^3-COSMO calculations. *Mol. Simul.* 34, 1013–1017. doi: 10.1080/08927020802235672

Tsuneda, T., Singh, R. K., Iiyama, A., and Miyatake, K. (2017). Theoretical Investigation of the H_2O_2-Induced Degradation Mechanism of Hydrated Nafion Membrane via Ether-Linkage Dissociation. *ACS Omega* 2, 4053–4064. doi: 10.1021/acsomega.7b00594

Viswanathan, V., Hansen, H. A., Rossmeisl, J., and Nørskov, J. K. (2012a). Universality in oxygen reduction electrocatalysis on metal surfaces. *ACS Catal.* 2, 1654–1660. doi: 10.1021/cs300227s

Viswanathan, V., Hansen, H. A., Rossmeisl, J., and Nørskov, J. K. (2012b). Unifying the $2e^-$ and $4e^-$ reduction of oxygen on metal surfaces. *J. Phys. Chem. Lett.* 3, 2948–2951. doi: 10.1021/jz301476w

Wang, N., Feng, L., Shang, Y., Zhao, J., Cai, Q., and Jin, P. (2016a). Two-dimensional iron-tetracyanoquinodimethane(Fe-TCNQ) monolayer: an efficient electrocatalysts for the oxygen reduction reaction. *RSC Adv.* 6, 72952–72958. doi: 10.1039/C6RA14339C

Wang, N., Liu, Y., Zhao, J., and Cai, Q. (2016b). DFT-based study on the mechanisms of the oxygen reduction reaction on Co(acetylacetonate)$_2$ supported by N-doped graphene nanoribbon. *RSC Adv.* 6, 79662–79667. doi: 10.1039/C6RA17651H

Wang, Y., Yuan, H., Li, Y., and Chen, Z. (2015). Two-dimensional iron-phthalocyanine (Fe-Pc) monolayer as a promising single-atom-catalyst for oxygen reduction reaction: a computational study. *Nanoscale* 7, 11633–11641. doi: 10.1039/C5NR00302D

Wannakao, S., Maihom, T., Kongpatpanich, K., Limtrakul, J., and Promarak, V. (2017). Halogen substitutions leading to enhanced oxygen evolution and oxygen reduction reactions in metalloporphyrin frameworks. *Phys. Chem. Chem. Phys.* 19, 29540–29548. doi: 10.1039/C7CP06187K

Xia, W., Mahmood, A., Liang, Z., Zou, R., and Guo, S. (2016). Earth-abundant nanomaterials for oxygen reduction. *Angew. Chem. Int. Ed.* 55, 2650–2676. doi: 10.1002/anie.201504830

Xia, Z., An, L., Chen, P., and Xia, D. (2016). Non-Pt nanostructured catalysts for oxygen reduction reaction: synthesis, catalytic activity and its key factors. *Adv. Energy Mater.* 6:1600458. doi: 10.1002/aenm.201600458

Xiao, B. B., Jiang, X. B., and Jiang, Q. (2016). Density functional theory study of oxygen reduction reaction on $Pt/Pd_3Al(111)$ alloy electrocatalyst. *Phys. Chem. Chem. Phys.* 18, 14234–14243. doi: 10.1039/C6CP01066K

Xiao, B. B., Liu, H. Y., Jiang, X. B., Yu, Z. D., and Jiang, Q. (2017). A bifunctional two dimensional $TM_3(HHTP)_2$ monolayer and its variations for oxygen electrode reactions. *RSC Adv.* 7, 54332–54340. doi: 10.1039/C7RA09974F

Xu, H., Cheng, D., Cao, D., and Zeng, X. C. (2018). A universal principle for a rational design of single-atom electrocatalysts. *Nat. Catal.* 1, 339–348. doi: 10.1038/s41929-018-0063-z

Yang, X., Zheng, Y., Yang, J., Shi, W., Zhong, J. H., Zhang, C., et al. (2017). Modeling Fe/N/C catalysts in monolayer graphene. *ACS Catal.* 7, 139–145. doi: 10.1021/acscatal.6b02702

Yin, P., Yao, T., Wu, Y., Zheng, L., Lin, Y., Liu, W., et al. (2016). Single cobalt atoms with precise N-coordination as superior oxygen reduction reaction catalysts. *Angew. Chem. Int. Ed.* 55, 10800–10805. doi: 10.1002/anie.201604802

Zagal, J. H., and Koper, M. (2016). Reactivity descriptors for the activity of molecular MN_4 catalysts for the oxygen reduction reaction. *Angew. Chem. Int. Ed.* 55, 14510–14521. doi: 10.1002/anie.201604311

Zhang, P., Hou, X., Liu, L., Mi, J., and Dong, M. (2015). Two-dimensional π-conjugated metal bis(dithiolene) complex nanosheets as selective catalysts for oxygen reduction reaction. *J. Phys. Chem. C* 119, 28028–28037. doi: 10.1021/acs.jpcc.5b09148

Zhang, Q., Mamtani, K., Jain, D., Ozkan, U., and Asthagiri, A. (2016). CO poisoning effects on FeNC and CNx ORR catalysts: a combined experimental-computational study. *J. Phys. Chem. C* 120, 15173–15184. doi: 10.1021/acs.jpcc.6b03933

Zheng, Y., Jiao, Y., Zhu, Y., Cai, Q., Vasileff, A., Li, L. H., et al. (2017). Molecule-Level g-C_3N_4 coordinated transition metals as a new class of electrocatalysts for oxygen electrode reactions. *J. Am. Chem. Soc.* 139, 3336–3339. doi: 10.1021/jacs.6b13100

Conflict of Interest Statement: The authors declare that the research was conducted in the absence of any commercial or financial relationships that could be construed as a potential conflict of interest.